

# A DIRECT NUMERICAL SIMULATION STUDY OF TWO-PHASE TURBULENT FLOW WITH LARGE-SIZED MULTIPLE BUBBLES IN A HORIZONTAL FLAT CHANNEL

**Sang Won Kim**

Complex Phenomena Unified Simulation Research  
Team, RIKEN Center for Computational Science  
7 Chome-1-26 Minatojima Minamimachi,  
Chuo Ward, Kobe, Hyogo, Japan  
sangwon.kim@riken.jp

**Nobuyuki Oshima**

Division of Mechanical and Aerospace Engineering  
Hokkaido University  
Nishi 8 Chome Kita 13 Jo, Kita Ward,  
Sapporo, Hokkaido, Japan  
oshima@eng.hokudai.ac.jp

**Yuichi Murai**

Division of Mechanical and Aerospace Engineering  
Hokkaido University  
Nishi 8 Chome Kita 13 Jo, Kita Ward,  
Sapporo, Hokkaido, Japan  
murai@eng.hokudai.ac.jp

**Hyun Jin Park**

Division of Mechanical and Aerospace Engineering  
Hokkaido University  
Nishi 8 Chome Kita 13 Jo, Kita Ward,  
Sapporo, Hokkaido, Japan  
park@eng.hokudai.ac.jp

## ABSTRACT

The horizontal turbulent channel flows with injected multiple large-sized bubbles are performed through direct numerical simulation. We study the drag reduction mechanism of large-sized bubbles by analyzing four different volumes of air, while the frictional Reynolds number is kept constant. We apply a VOF model to compute the two immiscible fluids water and air, the sharp interface between fluids captured by the isoAdvector method. We established our simulation setup using experimental data to compare with it in further studies. Simulation results show that the drag reduction ratio is independent of the void fractions ratio. From the instantaneous bubble shapes and skin friction contours, the higher drag reduction occurs at the liquid film regime of sufficiently longer bubbles in the streamwise direction. Thus, an additional parameter such as streamwise bubble length is shown to influence the drag reduction mechanism.

## INTRODUCTION

Bubble drag reduction has been researched for over 40 years and applied to liquid transport in pipelines and ship surfaces in water. This method does not damage the environment compared to other techniques and does not require appendages or modifications on the wall surface. A mostly investigated situation of drag reduction by the air bubble injection involves microbubbles smaller than 1 mm. Since the first report by McCormick and Bhattacharyya (1973), many researchers have conducted experiments on micro-bubble drag reduction to study the parameter dependency and skin friction reduction process (Madavan et al. (1985); Kato et al. (1999)).

Meanwhile, Moriguchi and Kato (2002), Shen et al. (2006) reported that the bubble size dependency on micro-bubbles drag reduction is no significant effect in the case of the high shear rate. This implies that bubble size is not required to be very small. Recently, the discussion on the drag reduction mechanism of the bubble was shifted to its deformability, by Moriguchi and Kato (2002), Lu et al. (2005). Although showing significant drag reduction from the experimental scale, this method has a problem with the persistence of drag

reduction from the downstream owing to that medium size of bubbles (2–3 mm) contained in microbubbles frequently coalesce in the shear layer and become large-sized bubbles (> 5 mm) in the downstream region. Therefore, the bubble size at downstream of microbubble methods is important in determining the total drag reduction, when considering the persistency of drag reduction along the streamwise direction.

However, the critical bubble size has not been determined. In this situation, the drag reduction performance of large-sized bubbles was found to be dependent on the bubble length (Murai et al., 2007). Oishi and Murai (2014) rigorously investigated and described influential characteristics such as the velocity gradient and  $u'v'$  contours related to the drag reduction of a single large-sized bubble. Park et al. (2019) experimentally investigated the film thickness of large-sized bubbles and BDR. Kim et al. (2020) numerically realized a single large-sized bubble and investigated the flow field around a large-sized bubble. Recently, Kim et al. (2021, 2022) reported bubble shape and skin friction characteristics as several series of large-sized bubble volumes.

In this study, a direct numerical simulation of large-sized bubbly flow in turbulent channel flow was performed to investigate the drag reduction mechanism of large-sized bubbles. we present four different cases as volumes of air increase whereas the frictional Reynolds number is kept constant for investigating drag reduction performance of large-sized bubbles independent with the effect of turbulent shear flows.

## NUMERICAL METHOD

In this study, the flow is considered incompressible, and the fluids are considered Newtonian. The governing equations in this study for continuity and momentum equation can be expressed by Eq. (1) and (2).

$$\nabla \cdot \mathbf{u} = 0 \quad (1)$$

$$\frac{\partial \rho \mathbf{u}}{\partial t} + \nabla \cdot (\rho \mathbf{u} \mathbf{u}) = -\nabla \cdot p + \nabla \cdot \mathbf{T} + \rho \mathbf{f} + \mathbf{f}_\sigma \quad (2)$$

In a two-phase flow, the integral form of the continuity equation can be expressed in Eq. (3) by change density term,  $\rho(\mathbf{x}, t)$ , because the density field has a discontinuity at the interface. The indicator field in Eq. (4) is defined to remove these insignificant parameters, and the integral form of the continuity equation is reformed as Eq. (5).

$$\frac{d}{dt} \int_V \rho(\mathbf{x}, t) dV = - \int_{\partial V} \rho(\mathbf{x}, t) \mathbf{u}(\mathbf{x}, t) \cdot d\mathbf{S} \quad (3)$$

$$H(\mathbf{x}, t) \equiv \frac{\rho(\mathbf{x}, t) - \rho_B}{\rho_A - \rho_B} \quad (4)$$

$$\frac{d}{dt} \int_{C_i} H(\mathbf{x}, t) dV = - \sum_{j \in B_i} S_{ij} \int_{F_j} H(\mathbf{x}, t) \mathbf{u}(\mathbf{x}, t) \cdot d\mathbf{S} \quad (5)$$

The left-hand side of Eq. (5) can be expressed by the volume fraction of fluid A in cell  $i$  as Eq. (6). On the other hand, the Right-hand side of Eq. (5) can be updated to total fraction during the time step,  $\Delta V_j(t, \Delta t)$ , as Eq. (7). From these equations, Eq. (5) can be expressed as Eq. (8).

$$\alpha_i(t) = \frac{1}{V_i} \int_{\Omega_i} H(\mathbf{x}, t) dV \quad (6)$$

$$\Delta V_j(t, \Delta t) \equiv \int_t^{t+\Delta t} \int_{F_j} H(\mathbf{x}, \tau) \mathbf{u}(\mathbf{x}, \tau) \cdot d\mathbf{S} d\tau \quad (7)$$

$$\alpha(t + \Delta t) = \alpha_i(t) - \frac{1}{V_i} \sum_{j \in B_i} S_{ij} \Delta V_j(t, \Delta t) \quad (8)$$

To simplify  $\Delta V_j(t, \Delta t)$  the term, some assumptions are needed in the *isoAdvector* method. The first assumption is  $u(x, \tau) \approx u(x, t)$ , which is regarding the velocity field as constant  $\tau$  during the interval of time step  $[t, t + \Delta t]$ . Another assumption is that  $u$  on the face  $F_j$  dotted with the differential face normal vector,  $d\mathbf{S}$ , can be approximated in terms of the constant volumetric face flux,  $\phi_j$ , as follows:

$$u(\mathbf{x}, t) \cdot d\mathbf{S} \approx \frac{\phi_j(t)}{|\mathbf{S}_j|} dS \quad (9)$$

The remaining surface integral is simply the instantaneous area of face  $j$  submerged in fluid A, which is called  $A_j(\tau)$  in Eq. (10). By using the above definition, Eq. (7) is now written as Eq. (11).

$$A_j(\tau) \equiv \int_{F_j} H(\mathbf{x}, \tau) dS = \int_{F_j \cap A(\tau)} dS \quad (10)$$

$$\Delta V_j(t, \Delta t) \approx \frac{\phi_j(t)}{|\mathbf{S}_j|} \int_t^{t+\Delta t} A_j(\tau) d\tau \quad (11)$$

The *isoAdvector* algorithm applied introduces a sub-grid scale model for estimating  $A_j(\tau)$  and intracellular distribution from the given volume fraction data to capture this local distribution information. The procedure of constructing the interface can be summarized as follows. (1) Find surface cells that contain volume fraction,  $0 < \alpha < 1$ . (2) Interpolate volume fraction of a vertex of surface cells from all surrounding cells. (3) Calculate face-interface intersection points between two vertexes. (4) Construct interface from intersection points and

lines in the surface cell, then split the cell and redistribute volume fraction so that sub-cells occupy  $\alpha = 1$  or 0. (5) Use the velocity field data to estimate interface motion during a time interval. By this procedure, suppressing numerical diffusion and precise advection can be achieved.

The numerical domain was modeled according to the experimental channel set-up of Oishi and Murai (2014). The length and width of the computational domain can be shortened by the periodic conditions in the streamwise and spanwise directions to save computational resources. Based on the experimental conditions, the domain dimensions were as follows: height ( $H = 2h$ ) = 10 mm, where  $h$  is the half-height of the channel, length ( $L$ ) = 100 mm, and width ( $W$ ) = 70 mm. Table 1 lists the experimental and numerical conditions of the present study, and a geometrical description of the numerical domain is shown in Fig. 1. The present study generated a turbulent Couette flow in the channel to compare the experimental results and realize similar flow conditions with ship surface.

Table 1. Experimental & numerical conditions.

	Oishi and Murai (2014)	Present study
$L \times H \times W$ [mm]	6000 × 10 × 100	100 × 10 × 70
$\rho$ [kg/m <sup>3</sup> ]	998.7	998.7
$U_{\text{mean}}$ [m/s]	1.0	1.11
$U_{\text{wall}}$ [m/s]	–	2.16
$Fr$	3.19	3.54
$Re$	9260	10278
$Re_\tau$	260	

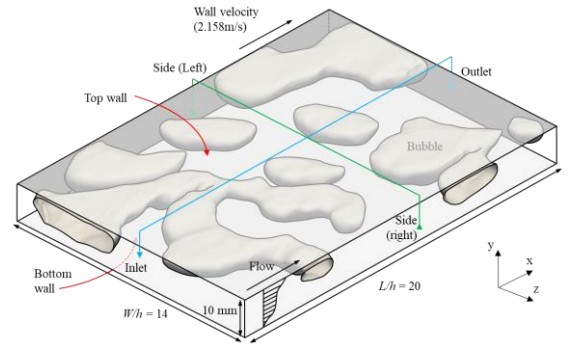


Figure 1. Schematic of the numerical conditions.

The velocity of the upper wall in the channel ( $U_{\text{wall}}$ ) for the Couette flow was adjusted to obtain the same friction velocity ( $u_\tau$ ) of the experimental study to compare the drag reduction ratio. All dimensionless numbers were obtained from single-phase flow conditions. Numerical simulation was performed using the open-source CFD package OpenFOAM@v2006. The *PimpleFoam* solver was used to generate a fully developed turbulent flow, whereas the *InterIsoFoam* solver implemented the *IsoAdvector* method for the interface sharpening method was used for two-phase flow. Further details, such as the verification work on *InterIsoFoam*, are presented in Kim et al. (2020).

All schemes in this study provide second-order accuracy. The global time step was set to  $2.0 \times 10^{-6}$  s to ensure that the Courant–Friedrichs–Lewy (CFL) number remained below 0.5; the interface CFL number was less than 0.3, in each simulation

case, because the interface CFL number frequently shot up above the unit owing to the breakup and coalescence of the bubble. Further, both solvers use the Pimple algorithm for pressure-velocity coupling in a segregated manner, which computes a velocity field to satisfy the continuity and momentum equations using an iterative procedure.

## NUMERICAL RESULTS

The numerical simulations are comprised of four cases as the volume fraction of air,  $\alpha_{vol}$ , as described in Table 2. All cases injected bubbles after the boundary layer is fully developed and additional transient calculations were performed to achieve a steady state after the bubble injection in the channel.

Table 2. Simulation cases for large-sized bubbly flows.

Flow condition	Case	$\alpha_{vol}$
Turbulent Couette flow	C9	0.0957 (9.57 %)
	C14	0.1436 (14.36 %)
	C19	0.1908 (19.08 %)
	C24	0.2469 (24.69 %)

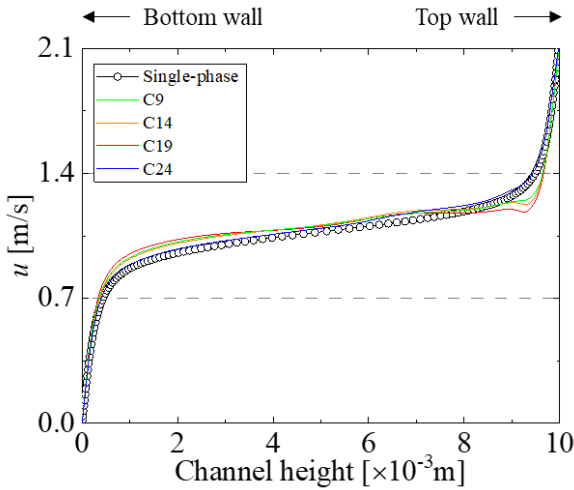


Figure 2. Mean velocity profile of bubble flow as volume fractions.

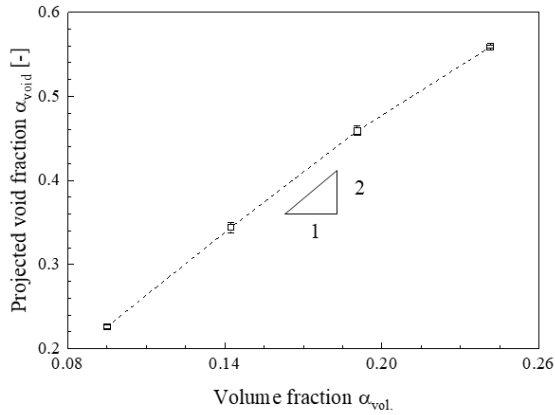


Figure 3. Relationship between volume fraction of air and Projected void fractions.

Figure 2 shows the mean velocity of the bubbly flow as the volume fraction of air. Mean velocity profiles were almost constant with showing small fluctuations and decreasing near the top wall owing to the existence of large-sized bubbles. With these trends, the velocities near the bottom wall slightly increased.

Figure 3 shows the relationship between the volume fractions and projected void fractions. The projected void fractions uniformly increased as volume fractions, and they were approximately twice the volume fractions. Figure 4 shows the relationship between the volume fractions and mean skin friction coefficients, where all plots indicate time-averaged values in 25ms. Consequently, similar trends are shown with each period, T1-T4, and the values are gradually decreased and converged skin friction as time passed. Typically, the drag reduction ratio is proportional as the projected void fraction increases. However, present results have not followed these trends. Thus, we investigated the instantaneous snapshot of bubble shapes and the contours of skin friction coefficient. Figures 5 and 6 show four typical samples of them, where the case numbers are assigned in chronological order.

As can be observed, the bubbles are coalesced and become larger as the volume fraction increases, and finally the flow state becomes to resemble a churn flow. From the contour of the skin friction coefficient, the liquid films of some large-sized bubbles, those are relatively small or aligned in a spanwise direction, show high skin friction similar to the region without the bubbles. Meanwhile, the liquid film of relatively large bubbles provides lower skin friction than that in other regions and the turbulent shear flow is disappeared in the regions. We expected that turbulent coherent structures are too large to intrude flows in liquid films and cause the relaminarization on that region, and such large bubbles are shown in C24 cases.

Moreover, by measuring the streamwise bubble length as spacing 1mm in spanwise direction, C24 clearly shows longer length distribution over 40mm while other cases are shown similar trends with each other, as shown in Figure 7. These trends are corresponding with those of skin friction coefficients.

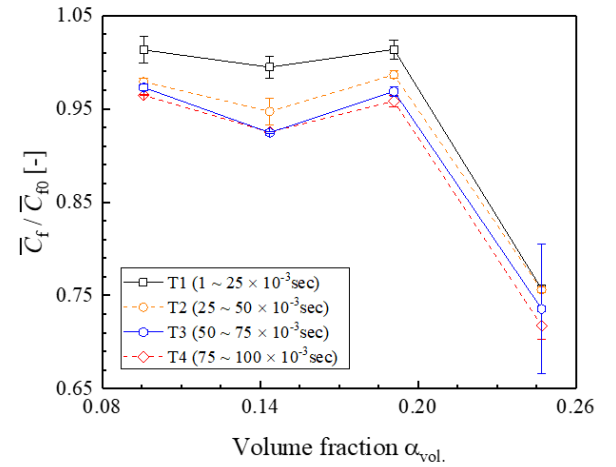


Figure 4. Mean skin friction coefficients as averaged period.

## CONCLUSION

In this study, a direct numerical simulation of the large-sized bubbly flow in turbulent channel flows was performed. The numerical results show reasonable even conducting simulations for longer periods. Interestingly, near-zero skin friction contours on the liquid film of the large-sized bubble are successfully confirmed from sufficiently large-sized bubbles, especially the C24 case, and this effect is maximized when the bubble reaches sufficiently longer in a streamwise direction.

## ACKNOWLEDGEMENTS

This Research and development work was supported by high-performance computing projects (hp 200223, 210160).

## REFERENCES

- McCormick, M., and Bhattacharyya, R., 1973. Drag reduction of a submersible hull by electrolysis. *Nav. Eng. J.* 85(2), 11–16.
- Madavan, N.K., Deutsch, S., and Merkle, C.L., 1984. Reduction of turbulent skin friction by microbubbles. *Phys. Fluids* 27(2), 356-363.
- Kato, H., Iwashina, T., Miyanaga, M., and Yamaguchi, H., 1999. Effect of microbubbles on the structure of turbulence in a turbulent boundary layer. *J. Marine Sci. Tech.* 4, 115-162.
- Moriguchi, Y., and Kato, H., 2002. Influence of microbubble diameter and distribution on frictional resistance reduction. *J. Mar. Sci. Technol.* 7(2), 79–85.
- Shen, X., Perlin, M., and Ceccio S.L., 2006. Influence of bubble size on microbubble drag reduction. *Exp. Fluids* 41, 415-24.
- Lu, J., Fernandez, A., and Tryggvason, G., 2005. The effect of bubbles on the wall drag in a turbulent channel flow. *Phys. Fluids* 17(9), 095102.
- Murai, Y., Fukuda, H., Oishi, Y., Kodama, Y., and Yamamoto, F., 2007. Skin friction reduction by large air bubbles in a horizontal channel flow. *Int. J. Multiphase Flow* 33(2), 147–163.
- Oishi, Y., and Murai, Y., 2014. Horizontal turbulent channel flow interacted by a single large bubble. *Exp. Therm. Fluid Sci.* 55, 128–139.
- Park, H.J., Tasaka, Y., and Murai, Y., 2019. Bubbly drag reduction investigated by time-resolved ultrasonic pulse echography for liquid films creeping inside a turbulent boundary layer. *Exp. Therm. Fluid Sci.* 103, 66–77.
- Kim, S.W., Oshima, N., Murai, Y., and Park, H.J., 2020. Numerical investigation of a single intermediate-sized bubble in horizontal turbulent channel flow. *J. Fluid Sci. Technol.* 15(3).
- Kim, S.W., Oshima, N., Murai, Y., and Park, H.J., 2021. Direct numerical simulation of frictional drag modulation in horizontal channel flow subjected to single large-sized bubble injection. *Int. J. Multiphase Flow*, 145, 103838.
- Kim, S.W., Oshima, N., and Park, H.J., 2022. Numerical flow visualization of a single large-sized bubble in turbulent Couette flow using OpenFOAM. *J. Vis.*, (Accepted).

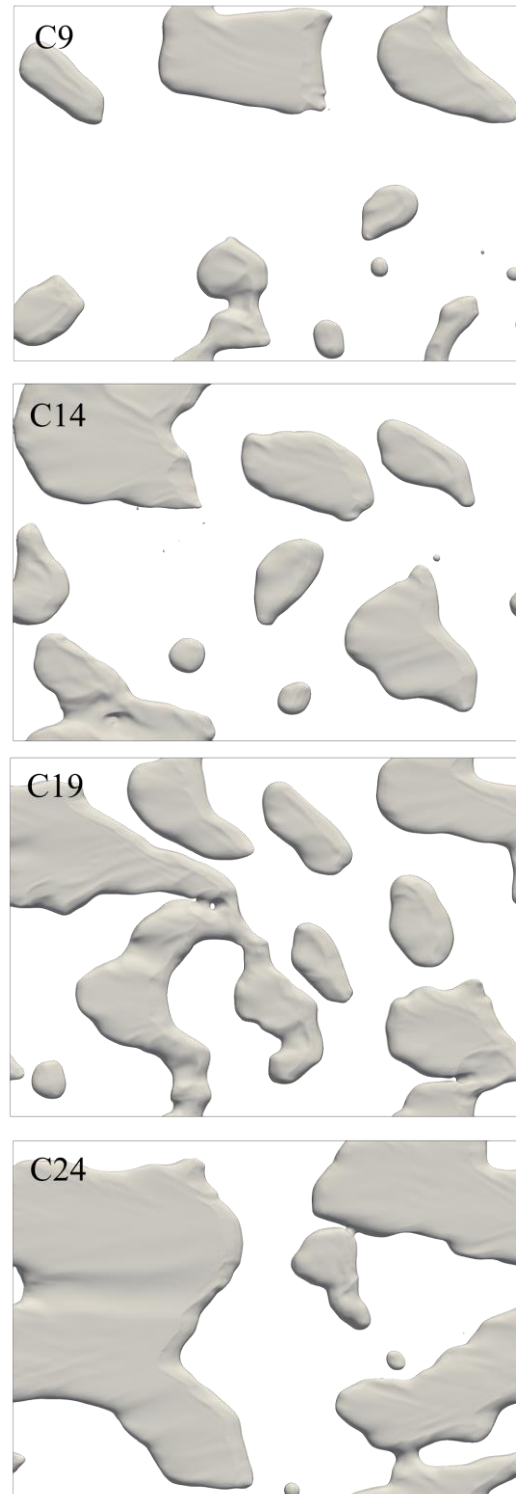


Figure 5. Instantaneous snapshot on bubble shapes.

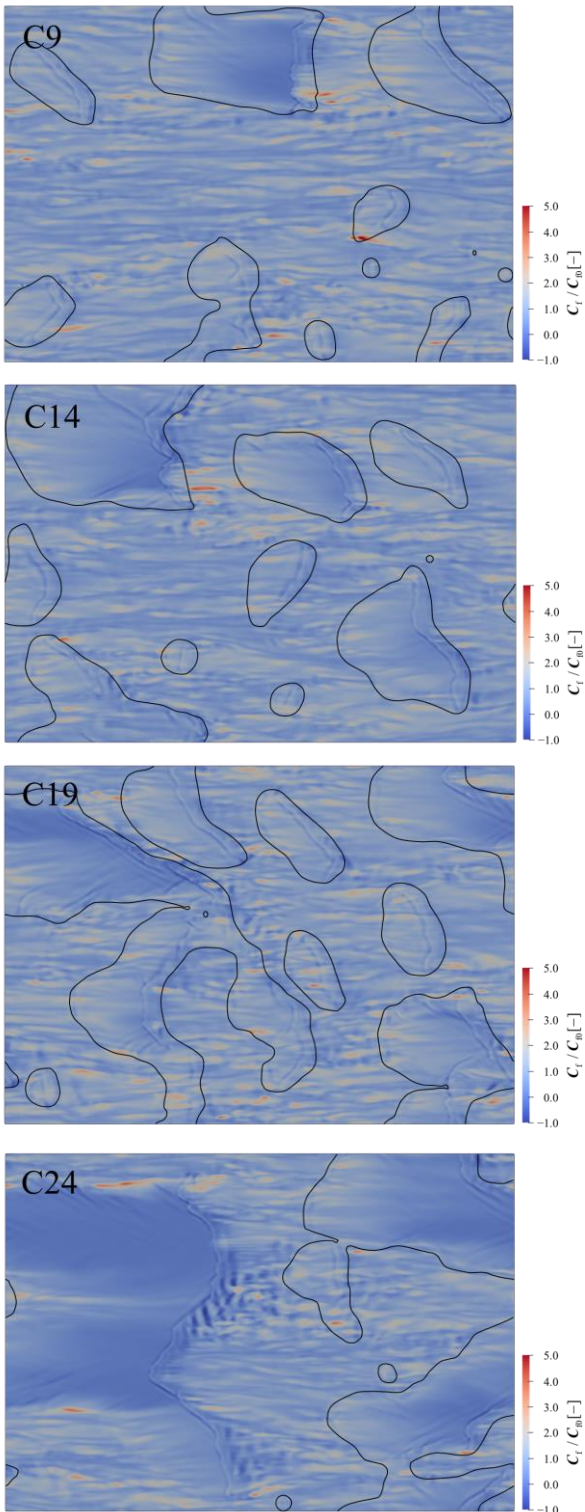


Figure 6. Instantaneous snapshot on contours of skin friction coefficients.

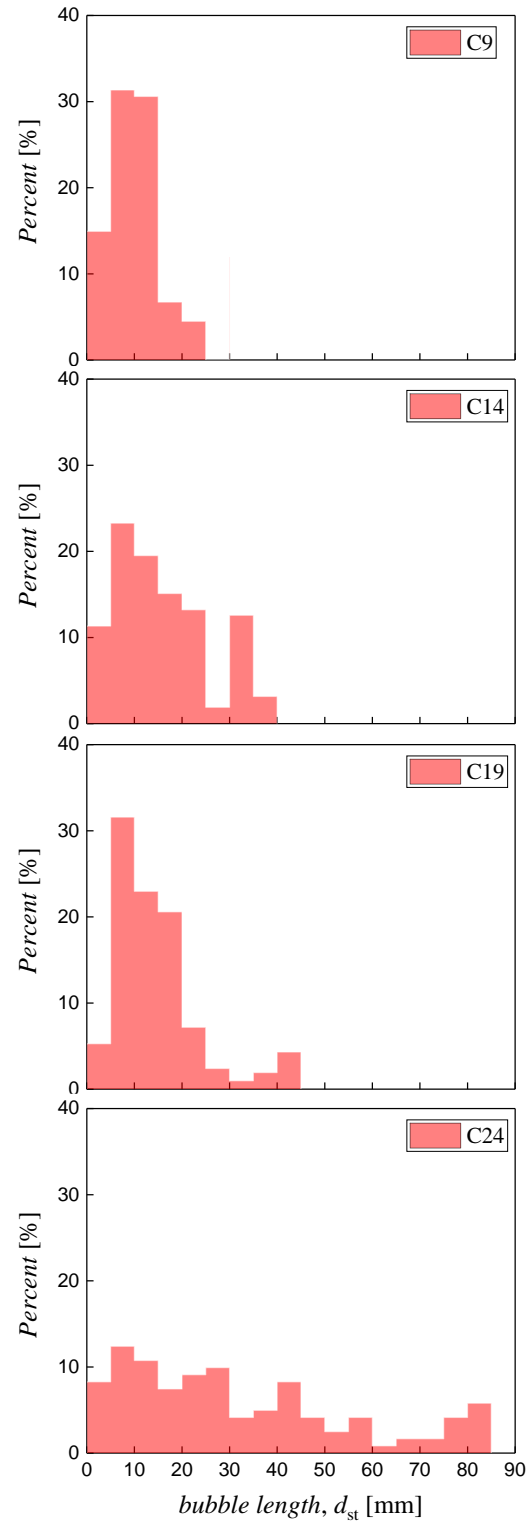


Figure 7. Instantaneous distributions of streamwise bubble length.